

# Atomic scale modeling of shock response of fused silica and $\alpha$ -quartz

J. Wang<sup>1</sup> · A. M. Rajendran<sup>2</sup> · A. M. Dongare<sup>1</sup>

Received: 26 May 2015 / Accepted: 26 August 2015 / Published online: 18 September 2015  
© Springer Science+Business Media New York 2015

**Abstract** Large-scale molecular dynamics (MD) simulations are carried out using the Tersoff potential to understand the shock wave propagation behavior and the microstructural response of amorphous silica (a-SiO<sub>2</sub>) and  $\alpha$ -quartz. The effect of shock pressure on the densification and phase transformation behavior is investigated using impact velocities of 0.5, 1.0, 1.5, and 2.0 km/s for a-SiO<sub>2</sub> and using impact velocities of 2.0 and 3.0 km/s for  $\alpha$ -quartz. MD simulations for a-SiO<sub>2</sub> suggest that impact velocities of 1.5 km/s and higher result in average pressures that are greater than 9 GPa for the compressed material leading to permanent densification of the material behind the shock front. In addition, the high peak pressures render a phase transformation of the amorphous phase to the high-pressure stishovite phase, and the microstructure corresponds to a heterogeneous mixture of stishovite and liquid SiO<sub>2</sub>. Spall failure due to the interaction of the reflected tensile waves, however, is not observed for any of the velocities considered for amorphous silica as the peak tensile pressure generated is insufficient to nucleate cracks. This is verified through MD simulations of uniaxial expansion of fused silica to compute the spall strength at the strain rates generated during shock simulations ( $10^9$  to  $10^{10}$  s<sup>-1</sup>). The uniaxial expansion simulations suggest a brittle mode of failure for a-SiO<sub>2</sub>, as observed

experimentally. In comparison, shock-induced densification and phase transformation behavior to the high-pressure stishovite phase are also observed for  $\alpha$ -quartz for an impact velocity of 3.0 km/s. The threshold pressures for the densification and phase transformation behavior for amorphous silica and  $\alpha$ -quartz compare very well with those observed experimentally.

## Introduction

The understanding of the deformation and failure response of ceramics comprising of covalent/ionic interactions under dynamic loading conditions has been of interest for several decades to investigate their stability and response in extreme environments, especially for applications in a majority of impact resistant structures [1]. The dynamic response of these materials is characterized by a large Hugoniot elastic limit (HEL), i.e., the shock pressure corresponding to dynamic yielding. The deformation behavior of these materials is largely attributed to modifications in local density, defect formation, phase transformation, etc., that can lead to crack nucleation and propagation to cause failure. The applicability of these materials for impact resistant applications, therefore, requires a fundamental understanding of the dynamic response of these materials under the shock-loading conditions at the atomic scales as well as the micromechanisms related to crack nucleation and propagation. The complex chemical structure of these materials and the plastic deformation behavior coupled with phase transformation behavior at high pressures and temperatures, however, make it difficult to determine the role of the individual contributions.

One such technologically important material is fused silica (SiO<sub>2</sub>) that has been studied extensively using

✉ A. M. Dongare  
dongare@uconn.edu

<sup>1</sup> Department of Materials Science and Engineering, Institute of Materials Science, University of Connecticut, Storrs, CT 06269, USA

<sup>2</sup> Department of Mechanical Engineering, University of Mississippi, University, MS 38677, USA

experiments as well as computational methods to investigate the deformation and phase transformation response at high temperatures and high pressures. Experimental studies [2–7] have suggested the densification of fused silica under shock-loading conditions at shock pressures above 9 GPa. The densification is attributed to the atomic rearrangement of the  $\text{SiO}_4$  tetrahedra under shock compression [5]. However, a shock pressure of 16 GPa is observed to be an upper limit for the densification process. The shock pressures ranging from 16 to 30 GPa correspond to the formation of a heterogeneous phase under shock compression. The heterogeneous phase comprises of a localized high-pressure phase of  $\text{SiO}_2$  and zones of  $\text{SiO}_2$  melt in the shock compressed region [8–10]. In comparison, the shock response of the crystalline stable phase of  $\text{SiO}_2$  ( $\alpha$ -quartz) is characterized by a higher HEL as compared to fused silica and a phase transition from  $\alpha$ -quartz to the high-pressure stishovite phase in the pressure range from 16 to 38 GPa [8–10]. This phase transformation, however, requires shock pressures of 40–50 GPa to complete. Lower shock pressure and/or short time scales may limit this phase transformation and the resulting material will have a fluid-like structure with a short range order.

Thus, the silica system proves to be a unique system to investigate the links between bonding environment, wave propagation behavior, shock pressures, and phase transformation behavior in brittle materials. The heterogeneous nature of these materials and the small time scales of the processes involved, however, make it difficult to identify and characterize the atomic scale processes using experiments alone. The recent advancements in the availability of computational resources and the atomic scale computational methods such as classical molecular dynamics (MD) allow for the investigation of these processes at the atomic resolution that may be instrumental in physical interpretation of experimental observations. The ability of MD simulation techniques to provide quantitative information on the atomic-level processes that determine the behavior and response of materials is largely defined by the availability of accurate and computationally efficient interatomic potentials. The embedded atom method (EAM) [11–13] is one example of a highly successful approach as it has established the framework for a group of potentials that are used in the majority of current simulations of metals and metallic alloys. As a result, MD simulations have been used to investigate the micromechanisms related to the deformation and failure response [14–19] of metals and metallic alloys at the atomic scales under high strain rates and shock-loading conditions.

The applicability of MD simulations to model the shock response of silicates, however, is rather limited. The bonding in silicate glasses (Si–O) is predominantly ionic and therefore the silica system is mostly modeled as an

ionic system with silicon cations and oxygen anions. As a result, the interatomic potentials for Si–O systems employ long-range Coulomb interactions using explicit point charges on the Si and O atoms. One such example is the Born–Mayer–Huggins (BMH) form that consists of long-range Coulomb interactions, the electron cloud repulsion, and the dipole–dipole and the dipole–quadrupole dispersion interactions. The BMH form is parameterized for silica by Tsuneyuki et al. [20] and van Beest et al. [21], and referred to as TTAM potential and BKS potential, respectively. These potentials require the evaluation of long-range Coulomb interactions and hence are computationally expensive for large-scale simulations. For example, a few studies have employed MD simulations to investigate the structural response under shock-loading conditions [22, 23]. While these studies have primarily focused on the investigation of the densification of the material under shock compression, the system size in these simulations is typically limited to up to tens of thousands of atoms using these long-range Coulomb potentials. As a result, the wave propagation behavior, the shock rise times, the propagation of the reflected waves, the phase transformation behavior, and the failure mechanisms have not been investigated using these potentials.

An alternative to the long-range interactions was developed by Munetoh et al. [24] in the functional form of the Tersoff potential [25] for the Si–O interactions. This formulation excludes the Coulomb interactions and incorporates a bond-order term that includes an angular dependence to account for the bonding environment. This exclusion of the long-range interactions allows for the modeling of large systems (tens of million atoms) with a reasonable computing expense. This parameterization is able to reproduce the structural energetics of the various crystalline phases as well as the amorphous phase for silica [24]. In addition, the parameterization has also been able to accurately reproduce the experimental Hugoniot curve for amorphous silica [26] thus making it suitable to model the dynamic response under shock-loading conditions. This parameterization is referred to as the “Tersoff” potential in this paper and is used for the shock simulations of silica systems reported here.

The goal of this paper is to investigate the ability of the Tersoff potential to model the response of fused silica under dynamic loading conditions using large-scale MD simulations. The amorphous silica sample is prepared by slowly heating and quenching an  $\alpha$ -cristobalite system to obtain a small piece of silica glass. Planar shock-loading conditions at various impact velocities are used to understand the effect of shock pressures on the deformation and phase transformation behavior of fused silica. In addition, the dynamic failure behavior of  $\alpha$ - $\text{SiO}_2$  is studied using conditions of uniaxial strain expansion at strain rates

between  $10^9$  and  $10^{10}$  s<sup>-1</sup>. The deformation and failure response of fused silica is compared to that for  $\alpha$ -quartz predicted using the Tersoff potential to gain insights into the effect of microstructure. The details of the simulation setup and analysis tools are described in the “[Computational details](#)” section, the wave propagation and phase transformation behavior in amorphous silica is discussed in the “[Shock response of a-SiO<sub>2</sub>](#)” section, the simulations to compute the spall strength of amorphous silica are discussed in “[Spall strength of a-SiO<sub>2</sub>](#)” section, and the results are compared with the shock response for  $\alpha$ -quartz in “[Shock response of crystalline phases of SiO<sub>2</sub> \( \$\alpha\$ -Quartz\)](#)” section.

## Computational details

The  $\alpha$ -cristobalite system comprising of 864 Si atoms and 1728 O atoms, and dimensions of 30.49 Å × 30.49 Å × 42.57 Å, is used to build the initial amorphous system. The  $\alpha$ -cristobalite system is first thermalized from 0.5 to 5000 K in 200 ps with a heating rate of 25 K/ps and then equilibrated at 5000 K for 200 ps at constant temperature and zero pressure (NPT ensemble using the Nose–Hoover algorithm) to obtain a fully liquid structure. The liquid SiO<sub>2</sub> is then quenched from 5000 K to room temperature 300 K with a cooling rate less than 13 K/ps to create the amorphous structure. The as-generated amorphous structure is then replicated to construct a large one for the shock-loading and uniaxial strain simulations followed by an equilibration for 50 ps to build the initial a-SiO<sub>2</sub> sample for the MD simulations. The simulations are performed using LAMMPS software [27] using a timestep of 1 fs and the velocity-Verlet algorithm [28] as the time integrator.

The density of the amorphous silica created using this method with the Tersoff potential is computed to be 2.312 g/cm<sup>3</sup>, which is in good agreement with other MD studies [29–32], varying from 2.04–2.38 g/cm<sup>3</sup> (Brutzel [29] 2.04 g/cm<sup>3</sup>, Muralidharan [30] 2.2–2.3 g/cm<sup>3</sup>, Yuan [32] 2.29–2.38 g/cm<sup>3</sup> depending on cutoff radius of short range interatomic radius, Mantisi [31] 2.18 g/cm<sup>3</sup>). The density of the created sample is also comparable to the experimental value of bulk silica glass, 2.20 g/cm<sup>3</sup> [32]. The partial radial distribution functions (RDFs) of Si–Si, Si–O, and O–O pairs as shown in Fig. 1 compare the structure of the as-created a-SiO<sub>2</sub> glass with that computed from the experimental structures as well as with the original Tersoff potential [24]. The RDFs are determined from the trajectories of the small a-SiO<sub>2</sub> glass sample of 2592 atoms. The first peaks, Si–Si pair at 3.13 Å, Si–O pair at 1.65 Å, O–O pair at 2.67 Å, and the coordination number of 3.92 for the S–O pair are consistent with the experimental data as well as Munetoh’s results [24]. The Tersoff

potential is thus able to reproduce the amorphous structure for fused SiO<sub>2</sub>. The simulations of the shock response of fused silica samples are discussed below.

Similarly, the cohesive energy per SiO<sub>2</sub> ( $E_{\text{coh}}$ ), density, lattice constants, and elastic constants of  $\alpha$ -quartz predicted by Tersoff potential are given in Tables 1 and 2 in comparison with that predicted using density functional theory calculations (DFT). The DFT calculations are carried out to investigate the densities required to achieve this transformation. DFT calculations are performed using the VASP code [35]. The exchange–correlation functional is treated within the Perdew–Burke–Ernzerhof (PBE) generalized gradient approximations (GGA) [36]. The atomic positions are relaxed until all components of the forces on each atom are reduced to values below 0.01 eV/Å, with a cutoff energy of 520 eV for the plane-wave expansions and a Monkhorst–Pack  $k$ -point mesh of  $9 \times 9 \times 9$ . Although Tersoff potential fits a slightly higher cohesive energy, the elastic constants, which are the curvature of the energy curve, are consistent with DFT results. Tersoff potential overestimates  $a$  yet underestimates  $c$  as compared to DFT, yielding a lower  $c/a$  ratio and density (around 5 %). The RDFs of Si–Si, Si–O, and O–O pairs of the alpha quartz are also generated using Tersoff potential and compared to DFT result. The first peaks, Si–Si pair at 3.05 Å, Si–O pair at 1.65 Å, O–O pair at 2.65 Å, agree excellent with the DFT result. The Tersoff potential is thus able to reproduce the structural energetics of alpha quartz.

## Shock response of a-SiO<sub>2</sub>

The investigation of the densification and phase transformation as observed experimentally requires a system large enough to allow wave propagation through the sample for a sufficient amount of time. As a result, the amorphous sample is prepared as discussed earlier with dimensions of 47.8 nm × 47.8 nm × 100 nm and corresponds to 15,925,248 atoms. The sample is periodic in the  $X$  and  $Y$  directions and free in the shock ( $Z$ ) direction. While these sizes are very small as compared to the experimental samples, the dimensions allow for the wave propagation behavior for tens of ps during compression, as well as reflection and interaction to cause spall failure [14, 18]. To achieve shock-induced deformation, the first 5 nm of the sample is chosen as the piston and given an inward velocity ( $U_p$ ) along the  $Z$  axis for 10 ps. The inward velocity impact results in a planar shock wave that travels with a velocity ( $U_s$ ) toward the rear surface. At the end of the shock pulse, the system is allowed to evolve to respond to the impact and this generates a tail of the pressure wave at the front end of the sample that follows the compressive wave toward the rear end of the sample.

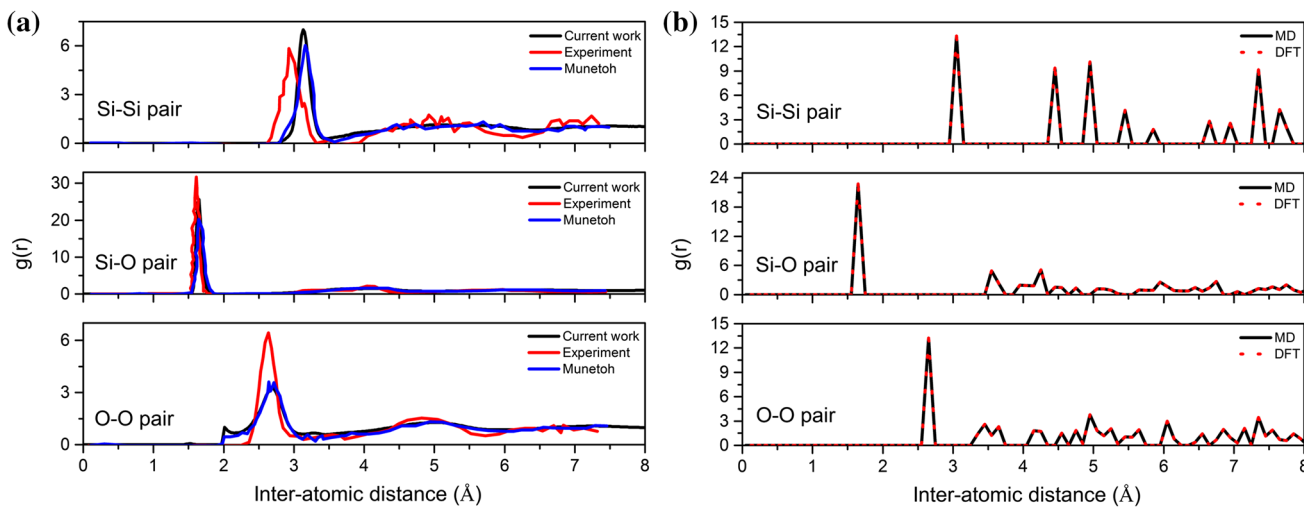


**Fig. 1 a** Partial radial distribution functions for the a-SiO<sub>2</sub> glass system. The *black solid line* represents the results from current work in comparison with the experimental data [24] as shown by the *dashed red line* and the original results using the Tersoff potential

[24] as shown by the *blue dashed line*. **b** Partial radial distribution functions for the α-quartz glass system as predicted using the Tersoff (*black line*) in comparison with that predicted using DFT simulations (Color figure online)

**Table 1** Lattice constants and density of α-quartz predicted by Tersoff potential in comparison with that predicted using DFT calculations

|         | α (Å) | c (Å) | c/a   | ρ (g/cc) |
|---------|-------|-------|-------|----------|
| MD-TF   | 5.08  | 5.28  | 1.039 | 2.42     |
| DFT-GGA | 4.97  | 5.46  | 1.100 | 2.56     |

To understand the temporal response of the glass to the shock wave propagation, the system is divided into sections along the Z axis and the values of pressure and velocity are averaged for all the atoms in each section. For example, a typical pressure (P) profile due to a piston velocity of 500 m/s along the Z direction as a function of time during the simulation is shown in Fig. 2. The peak shock wave pressure for an impact velocity of 500 m/s is calculated to be 4.4 GPa and the pressure in the material behind the shock front also remains constant as shown by the red contour. The tail of the pressure wave at the end of the shock pulse (10 ps) propagates through the shock compressed region toward the rear surface and returns the material to near zero pressure. The shock front reaches the rear surface and the compressed material begins to expand freely. The wave is thus reflected as a tensile wave which then interacts with the tail of the initial pressure wave. This

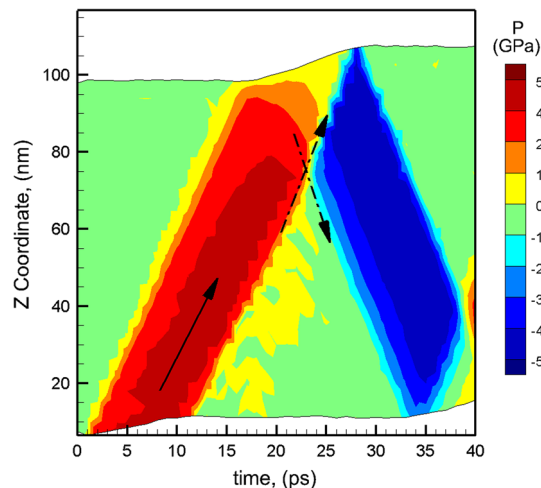


**Fig. 2** Contour plot of pressure as a function of Z coordinate of the sample and time during shock loading using an impact velocity of 0.5 km/s and a 10 ps square pulse. The *red* positive values correspond to compressive pressure and the negative values correspond to tensile pressures (Color figure online)

interaction (as shown by the dashed black lines) results in a triaxial state of tensile stress that propagates toward the front surface. The spall failure typically initiates at the location of the peak value of the tensile pressure generated

**Table 2** Cohesive energy and elastic constants for of α-quartz predicted by Tersoff potential in comparison with that predicted using DFT calculations

|         | E <sub>coh</sub> (eV) | C <sub>11</sub> (GPa) | C <sub>12</sub> (GPa) | C <sub>33</sub> (GPa) | C <sub>44</sub> (GPa) |
|---------|-----------------------|-----------------------|-----------------------|-----------------------|-----------------------|
| MD-TF   | −20.09                | 100.53                | 36.70                 | 87.97                 | 37.94                 |
| DFT-GGA | −24.07                | 92.26                 | 41.46                 | 99.83                 | 41.46                 |

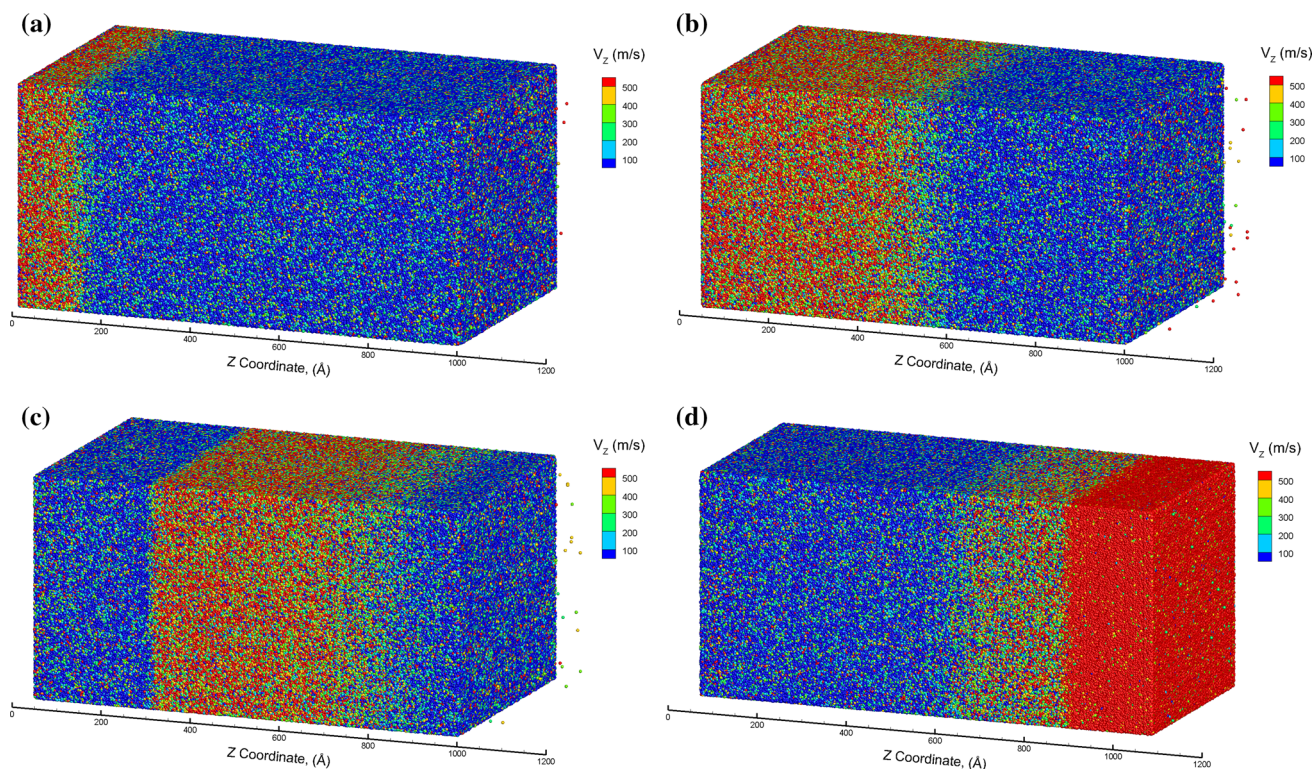


**Fig. 3** Evolution of the microstructure of a-SiO<sub>2</sub> during shock loading at an impact velocity of 0.5 km/s at times of **a** 3 ps, **b** 10 ps, **c** 15 ps, and **d** 25 ps. The atoms are colored according to the velocity in the shock direction (Color figure online)

due to the interaction of the reflect wave with the tail. The snapshots of the system at intermediate times are shown in Fig. 3a–d with the atoms colored according to the velocity in the shock direction. No failure of the sample is observed under the action of the reflected tensile wave at an impact velocity of 500 m/s.

MD simulations are carried out for impact velocities of 1.0, 1.5, and 2.0 km/s and a constant shock pulse of 10 ps to investigate the effect of shock pressures on the wave propagation and failure behavior. The contour plots of the pressure along the length of the sample in the shock direction for impact velocities of 0.5, 1.0, 1.5, and 2.0 km/s are presented as a function of time in Fig. 4a, b, c, d, respectively. It can be seen from the contour plots that higher impact velocities generate higher shock pressures due to larger compression of the material in the shocked region. The peak shock pressures generated for impact velocities of 0.5, 1.0, 1.5, and 2.0 km/s are observed to be 4.4, 7.7, 12.3, and 20.1 GPa, respectively. However, these peak pressures occur over a short period of time and are also experienced by very small regions of the sample as can be seen in the contour plots in Fig. 4. As a result, the compressed material between the shock front and the tail of the pressure wave experiences an average pressure that is much lower than the peak value generated. These lower values of the average pressure in the compressed material

(less than 9 GPa) during the propagation of the compressive wave allow the material to be brought back to near zero pressure by the propagation of the tail of the pressure wave for impact velocities of 0.5, 1.0, and 1.5 km/s. The regions that experience the peak values of pressure greater than 9 GPa at 1500 m/s are likely to undergo permanent densification locally through modifications in the SiO<sub>4</sub> tetrahedra under shock compression [5], but do not result in high overall residual compressive pressures in the contour plot in Fig. 4c. An impact velocity of 2.0 km/s, on the other hand, generates a significantly high value of the peak pressure of 20.1 GPa and an average pressure that is greater than 9 GPa in the material between the shock front and the tail. This value of the average pressure in the material results in a permanent densification of the material as shown by the residual compressive pressure (1–4 GPa) in the sample after the propagation of the tail of the pressure wave. Given the fact that permanent densification is found at 9 GPa experimentally [5], these contour plots suggest that a shock pulse of 10 ps is not enough to induce permanent densification of amorphous silica behind the shock front for impact velocities of 0.5, 1.0, and 1.5 km/s. A longer shock pulse can be expected to compress the material for longer times resulting in higher values of the average pressure in the material between the shock front and the tail. Also, for the case of the impact velocity of

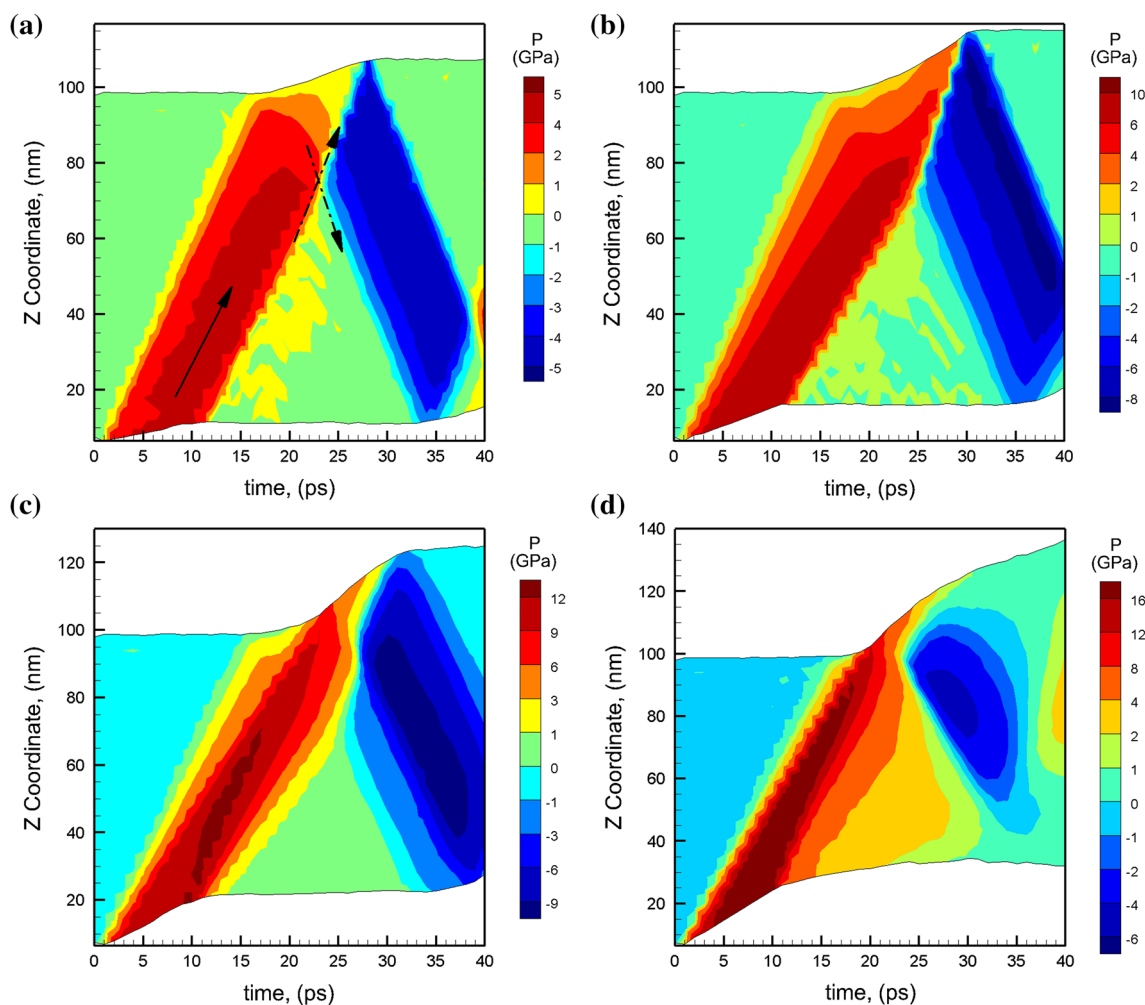


**Fig. 4** Pressure contours of a-SiO<sub>2</sub> during shock loading for impact velocities of **a** 0.5 km/s, **b** 1.0 km/s, **c** 1.5 km/s, and **d** 2.0 km/s (Color figure online)

2.0 km/s, the peak pressure generated falls above the experimentally observed limit of permanent densification (16 GPa) and therefore is expected to result in the formation of a heterogeneous mixture comprising of a high-pressure liquid phase and a high-pressure SiO<sub>2</sub> phase observed experimentally.

To investigate the microstructural response, the snapshots of the microstructure of the system at the end of the shock pulse (10 ps) are shown in Fig. 5a, b, c, for impact velocities of 1.0, 1.5, and 2.0 km/s, respectively, with the atoms colored according to the velocity in the shock direction. It can be seen from the particle velocities that the width of the shock front decreases as the impact velocity increases and has a very sharp shock front for an impact velocity of 2 km/s. The sufficiently high pressures at impact velocities of 1.5 and 2.0 km/s induce plastic deformation and local permanent densification of the material through modifications in the SiO<sub>4</sub> tetrahedra under shock compression [5]. This behavior affects the

propagation of the pressure wave as the material is being deformed and results in a decrease in the width of the constant pressure zone. As a result, a longer tail of the pressure wave is observed at the higher impact velocities. The snapshots of the microstructure of the system at the time of 15 ps are shown in Fig. 6a, b, c, for impact velocities of 1.0, 1.5, and 2.0 km/s, respectively. A time of 30 ps (as shown in the contour plots Fig. 4) corresponds to the peak of the tensile pressure generated by the interaction of the reflected tensile wave and the tail of the pressure wave. The peak tensile pressure increases with impact velocity up to a value of 10.5 GPa at an impact velocity of 1.5 km/s. The snapshot of the material is shown in Fig. 7a. This peak tensile pressure, however, does not result in failure of fused silica under the action of the reflected tensile waves (spallation). A further increase in impact velocity to 2.0 km/s, however, results in a reduced peak tensile pressure of 4.9 GPa at a time of 30 ps. The reduced pressure is due to the propagation of the reflected tensile

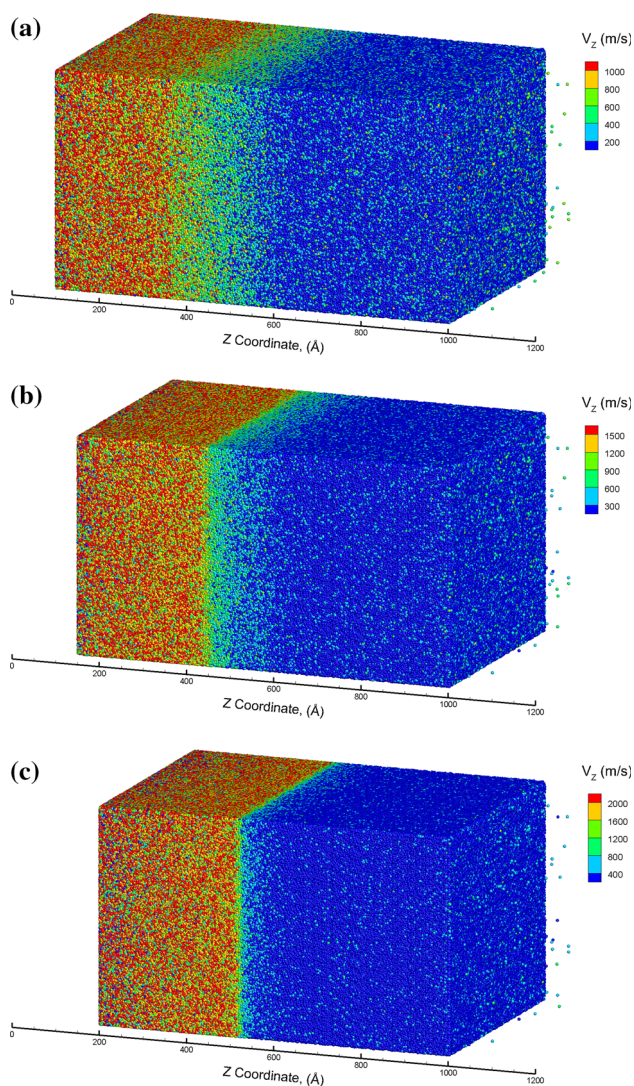


**Fig. 5** Evolution of the microstructure of a-SiO<sub>2</sub> during shock loading at time of 10 ps for impact velocity of **a** 1.0 km/s, **b** 1.5 km/s, and **c** 2.0 km/s. The atoms are colored according to the velocity in the shock direction (Color figure online)

waves through material that has undergone permanent densification (as shown by the orange region in Fig. 4d). In addition, sufficiently high pressures generated (greater than 16 GPa) result in the creation of a high-pressure liquid regions in the shock compressed region and the microstructure corresponds to a heterogeneous mixture of high pressure SiO<sub>2</sub> and liquid SiO<sub>2</sub>. The formation of the heterogeneous mixture is confirmed in the snapshots of the material shown in Fig. 7b, c at 30 and 40 ps, respectively, that show the material being ejected out of the system at the front end of the sample under the action of the reflected tensile pressure wave. This melting of the shocked region is not observed at impact velocities of 1.5 km/s and below as the peak shock pressures generated do not exceed 16 GPa. Thus, the threshold of the shock pressure required to

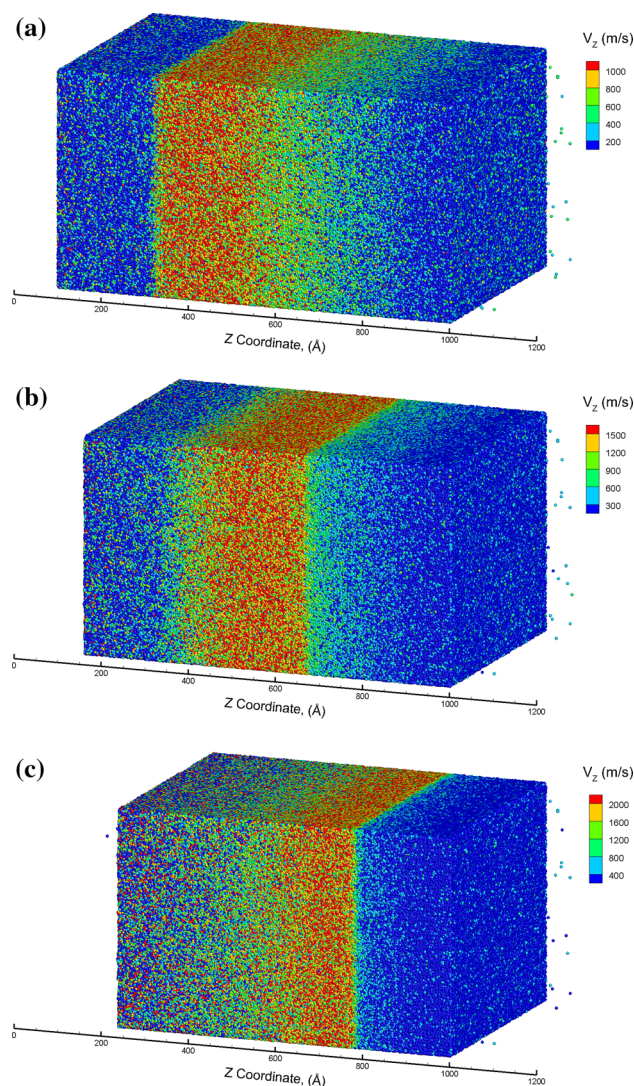


**Fig. 6** Snapshots of the microstructure of a-SiO<sub>2</sub> during shock loading at time of 15 ps for impact velocity of **a** 1.0 km/s, **b** 1.5 km/s, and **c** 2.0 km/s. The atoms are colored according to the velocity in the shock direction (Color figure online)

initiate melting of the material to form the heterogeneous phase as predicted using the Tersoff potential is consistent with that observed experimentally [8–10].

The high-pressure solid SiO<sub>2</sub> phase in this heterogeneous mixture has been speculated to be the stishovite phase [8–10]. This phase mixture can be investigated by plotting the density of the material along the length of the sample in the shock direction at the end of the shock pulse for various impact velocities as shown in Fig. 8 in comparison with the variation of the pressure along the length of the sample. It can be seen from these plots that the density of the shock compressed material reaches a value of  $\sim 3.6$  g/cm<sup>3</sup> for an impact velocity of 2.0 km/s. However, it is not clear if the compressed material corresponds to transformation to the stishovite phase. To investigate

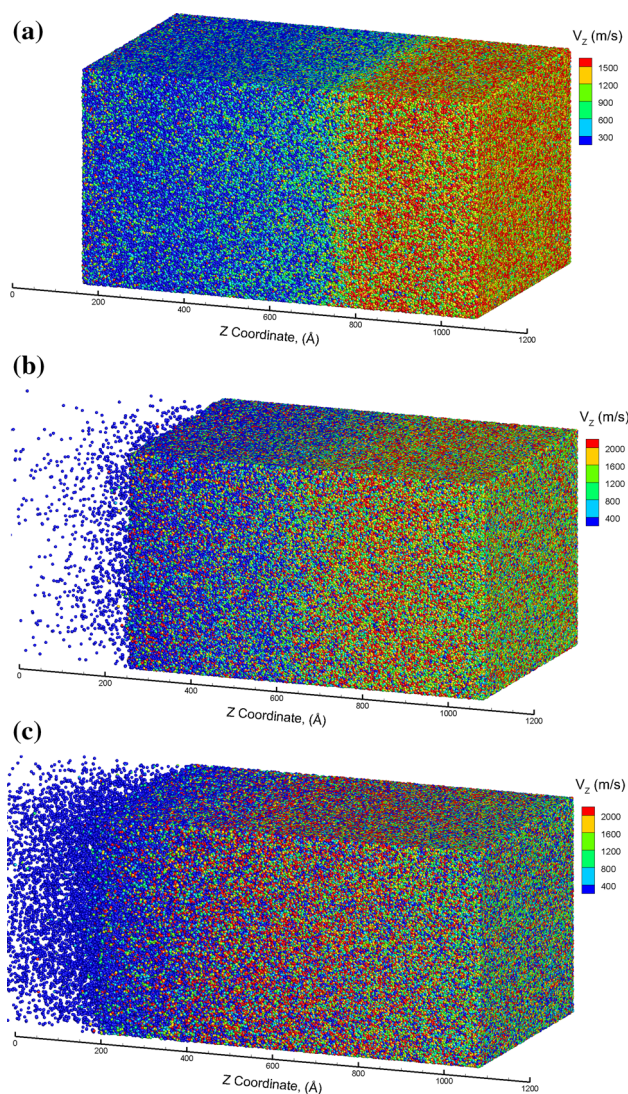


**Fig. 7** Snapshots of the microstructure of a-SiO<sub>2</sub> during shock loading at time of 30 ps for impact velocity of **a** 1.5 km/s, **b** 2.0 km/s, and **c** at time of 40 ps for velocity of 2.0 km/s. The atoms are colored according to the velocity in the shock direction (Color figure online)

the transformation behavior, the variation of the energy for the amorphous silica and the stishovite phase per molecule of SiO<sub>2</sub> as computed for the Tersoff potential is plotted as a function of density in Fig. 9. It can be seen from these plots that the MD simulation’s calculations predict that when amorphous silica is compressed to a density higher than 3.05 g/cm<sup>3</sup>, the material favors to transform to the stishovite phase as it has a lower energy as compared to amorphous silica. The MD simulations thus confirm that the heterogeneous mixture generated above shock pressures of 16 GPa corresponds to the high-pressure stishovite phase and a high-pressure liquid phase. The spall strength of fused silica using MD simulations of uniaxial expansion is computed below.

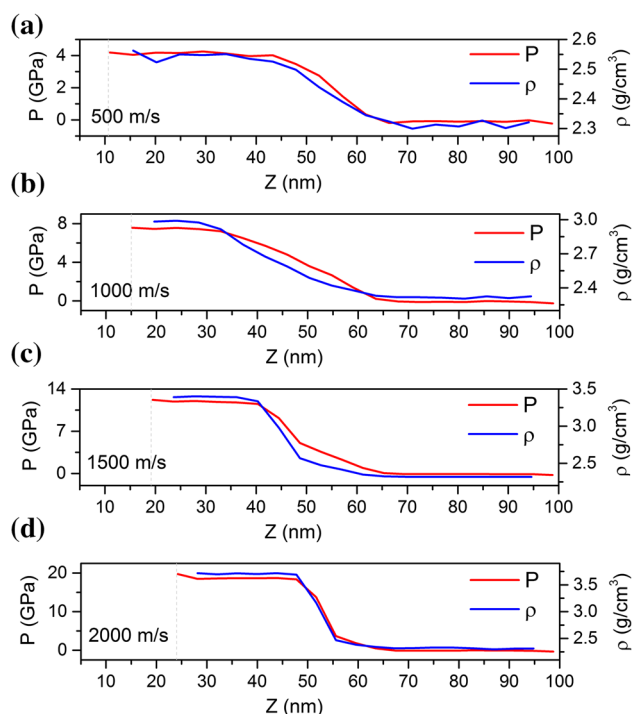


**Fig. 8** The densification of the system along with the pressure profile along the length of the sample in the shock direction at the end of the shock pulse (10 ps) for an impact velocity of **a** 500 m/s, **b** 1000 m/s, **c** 1500 m/s, and **d** 2000 m/s (Color figure online)

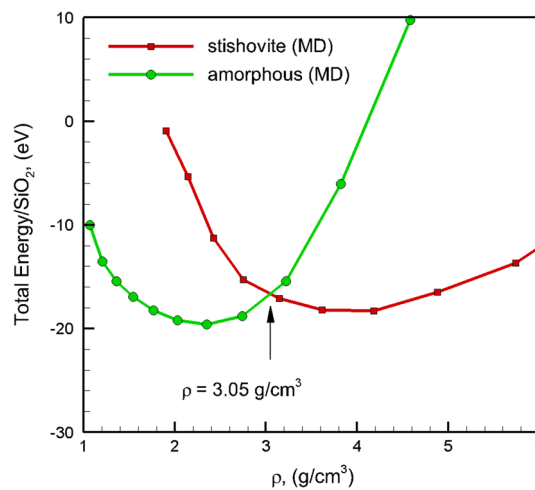


**Fig. 9** Plot of the energy of the amorphous and stishovite phases for silica as a function of density as computed for the Tersoff potential. The density of the amorphous-to-stishovite transformation is calculated to be 3.05 g/cm<sup>3</sup> for the Tersoff potential (Color figure online)

### Spall strength of a-SiO<sub>2</sub>

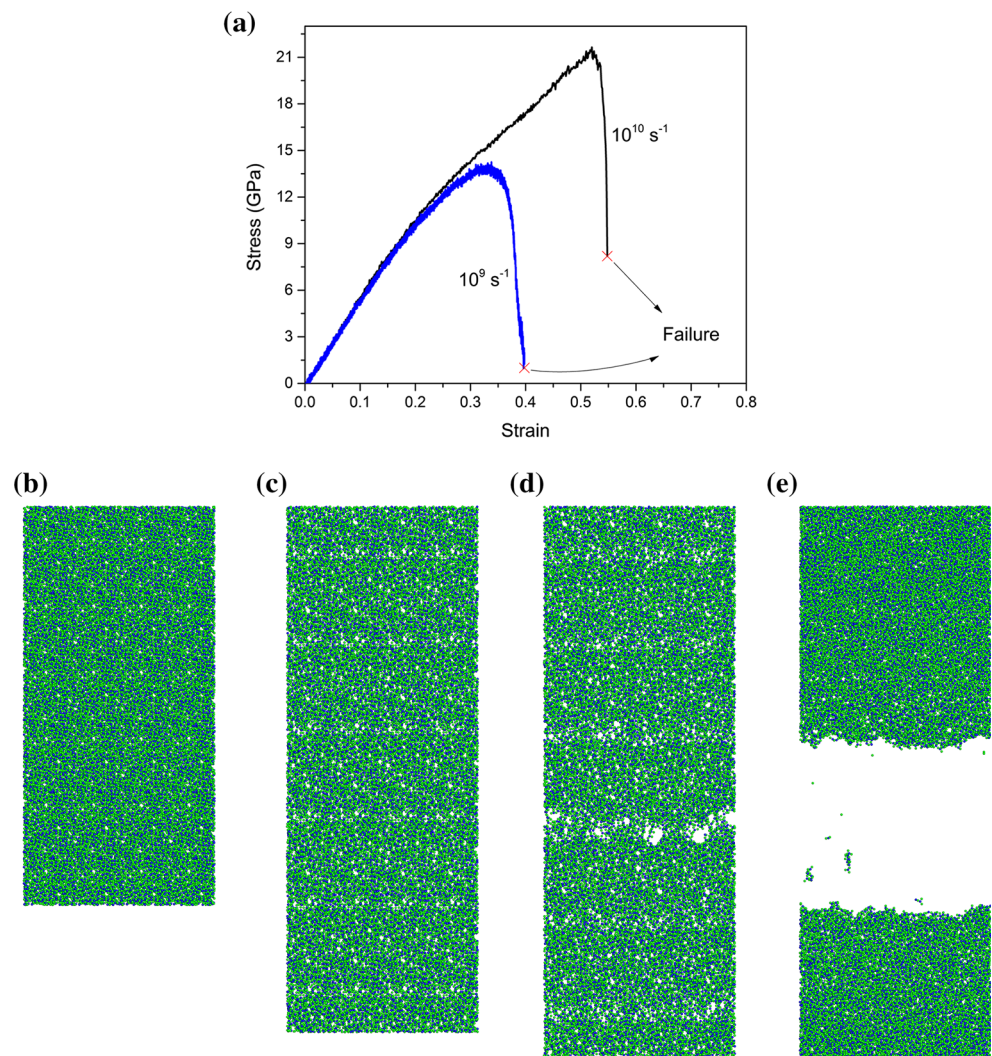
The shock simulations discussed above in “Shock response of a-SiO<sub>2</sub>” section do not result in spall failure under the triaxial state of tensile stress generated during the propagation of the reflected tensile waves. To understand the



dynamic failure behavior for a-SiO<sub>2</sub>, MD simulations of uniaxial expansion simulations are carried out to determine the spall strength of a-SiO<sub>2</sub> as well as the failure mechanisms. The rear surface velocity profiles computed from the shock simulations discussed above can be used to determine the strain rates experienced by the material [14] and suggest strain rates ranging from 10<sup>9</sup> to 10<sup>10</sup> s<sup>-1</sup>. The spall strength of a-SiO<sub>2</sub> is therefore calculated at these strain rates. An amorphous system with dimensions of 12 nm × 12 nm × 25 nm and 248,832 atoms and periodic in all directions is created using the method discussed in “Computational details” section. The initial snapshot of the material illustrating the microstructure of the system is shown in Fig. 3a, wherein the blue atoms are Si atoms and the green atoms are the O atoms. Deformation under conditions of uniaxial expansion ( $\varepsilon_x = \varepsilon_y = 0$ , and  $\varepsilon_z = \varepsilon$ ) is achieved by adjusting the coordinates in the loading direction (Z) of all of the atoms with a scaling parameter at each time step to define the strain rate of deformation. The

coordinates of the atoms in the X and Y directions are not scaled, thus resulting in zero strains in the X and Y directions. The evolution of the average stress in the loading direction as a function of strain in the loading direction is plotted in Fig. 10a for strain rates of 10<sup>9</sup> and 10<sup>10</sup> s<sup>-1</sup>. The stress–strain curves are initially linear and overlap each other in the elastic region for both the strain rates considered. The transition of the deformation from elastic to plastic behavior at both the strain rates is observed in the deviation from linear behavior for both the curves. The stress values are observed to increase to a peak value after which an abrupt decrease is observed. The abrupt decrease in the stress values corresponds to the nucleation of a crack that propagates perpendicular to the loading direction, immediately causing complete failure [14]. The snapshot in Fig. 10c at a strain of 37 % shows no voids/cracks forming in the sample. However, as shown by the snapshot in Fig. 10d, failure is observed to initiate by the planar nucleation of several voids that grow and coalesce

**Fig. 10** **a** The stress–strain curve of a-SiO<sub>2</sub> at strain rates of 10<sup>9</sup> s<sup>-1</sup> (blue) and 10<sup>10</sup> s<sup>-1</sup> (black). The snapshots of the microstructure of a-SiO<sub>2</sub> during uniaxial expansion at a strain rate of 10<sup>9</sup> s<sup>-1</sup> at **b** 0 % strain, **c** 37 % strain, **d** 38 % strain, and **e** 39 % strain. The blue atoms are Si atoms and the green atoms are the O atoms (Color figure online)



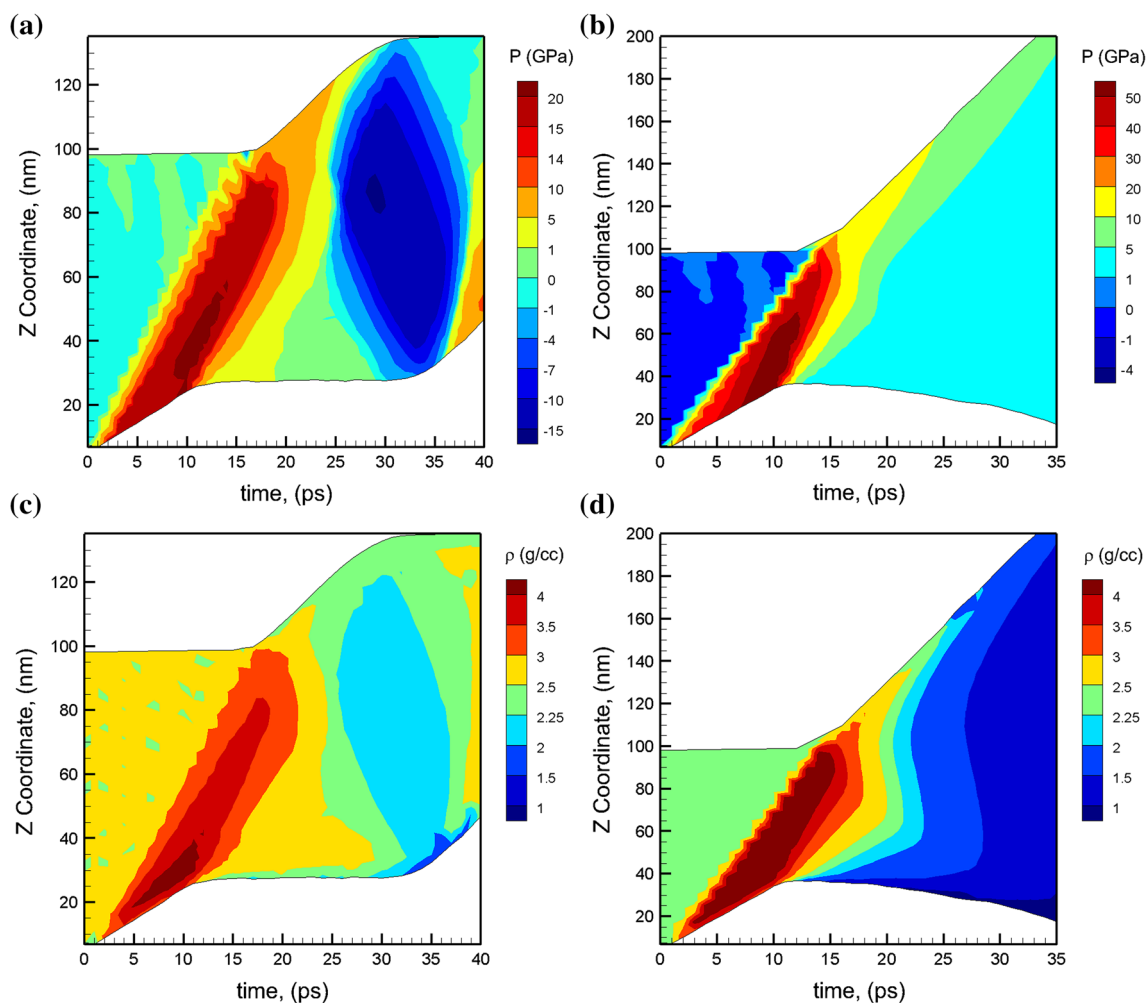


**Fig. 11** Pressure a contours of  $\alpha$ -quartz during shock loading for an impact velocities of **a** 2.0 km/s and **b** 3 km/s. The corresponding density contours are shown in **(c)** and **(d)**, respectively (Color figure online)

catastrophically along a plane that is perpendicular to the loading direction as shown in Fig. 10e at a strain of 39 %. The short time duration of crack nucleation, growth, and coalescence indicates a catastrophic brittle mode of failure as observed experimentally. The peak value of the tensile stress prior to crack nucleation is therefore defined as the spall strength of the material. The spall strength of amorphous silica using the Tersoff potential is computed to be 13.9 GPa at a strain rate of  $10^9 \text{ s}^{-1}$  and this strength increases to 21.5 GPa at a strain rate of  $10^{10} \text{ s}^{-1}$ . These computed values compare well with values ranging from 15 to 20 GPa computed using BKS potentials [30, 32–34]. The failure behavior predicted using BKS potentials, however, is characterized by a mechanism of slow growth and coalescence of voids suggesting a ductile mode of failure rather than a brittle mode of failure [33]. The capability of the Tersoff potential to model the shock response of  $\alpha$ -quartz is discussed below.

### Shock response of crystalline phases of $\text{SiO}_2$ ( $\alpha$ -Quartz)

As discussed before, the shock response of  $\alpha$ -quartz is characterized by a higher HEL as compared to fused silica as well as a phase transition from  $\alpha$ -quartz to the high-pressure stishovite phase in the pressure range from 16 to 38 GPa [8–10]. While the high-pressure phase transition is observed to initiate at these pressures, the phase transformation does not complete till shock pressures of 40–50 GPa are reached. As a result, a fluid-like structure with a short range order may be created at low pressures or at short time scales.

As a result, this study is extended to model the shock response of  $\alpha$ -quartz. The  $\alpha$ -quartz system for shock simulation is built with dimensions of  $50.17 \text{ nm} \times 50.31 \text{ nm} \times 100.61 \text{ nm}$  and 18,486,468 atoms. The shock simulations are carried out for piston velocities of 2.0 and

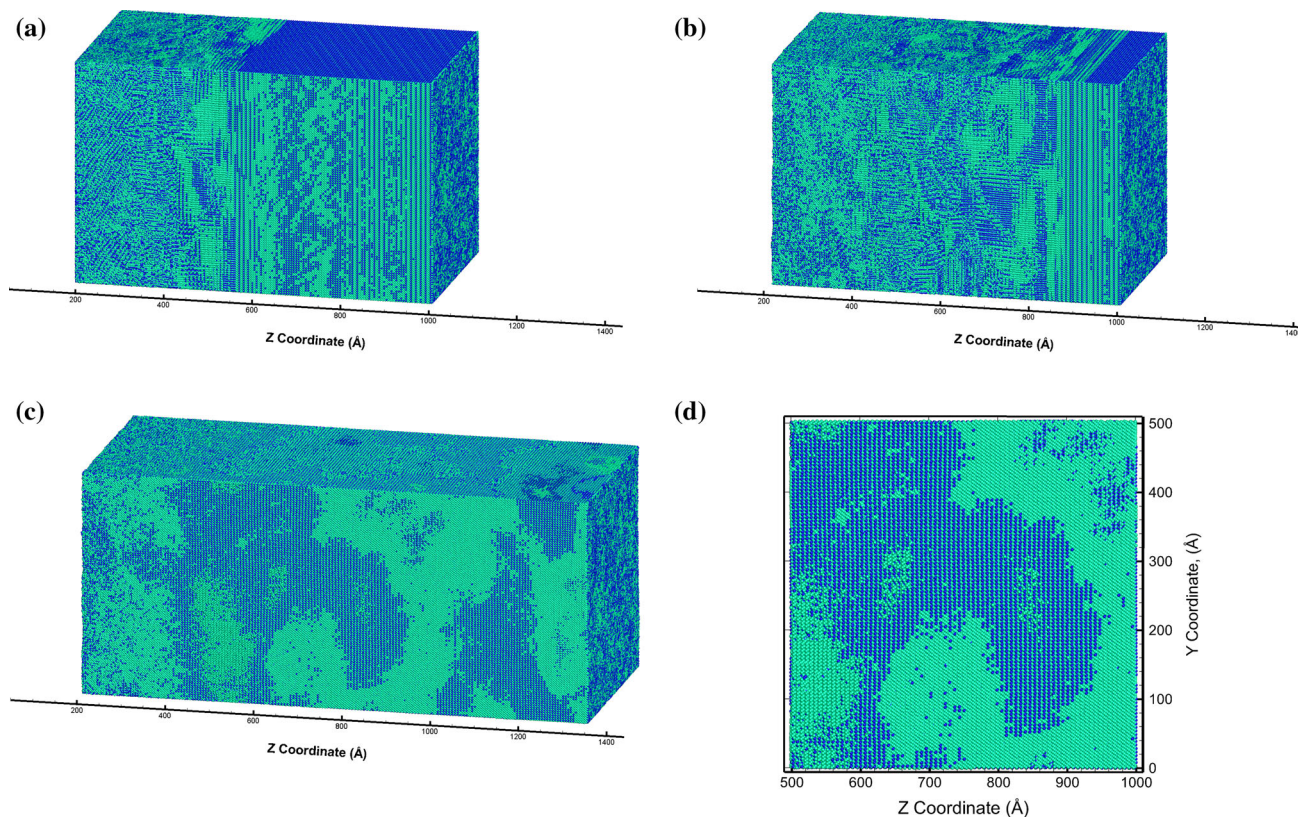


**Fig. 12** Evolution of the microstructure of  $\alpha$ -quartz during shock loading at an impact velocity of 2.0 km/s at times of **a** 10 ps, **b** 15 ps, and **c** 30 ps. The shock direction is shown by the *red arrow*. The *blue*

atoms are Si atoms and the *green* atoms are the O atoms. A detailed view of the microstructure of the snapshot in (c) showing the formation of grains is shown in (d) (Color figure online)

3.0 km/s using a square pulse of 10 ps as carried out for amorphous silica in “Shock response of a-SiO<sub>2</sub>” section. The contour plots of the pressure and density along the length of the sample in the shock direction for  $\alpha$ -quartz for an impact velocity of 2 km/s are plotted as a function of time in Fig. 11a, b, respectively. It can be seen from these plots that while a peak pressure of >18 GPa is reached during the shock compression, the material in the shock compressed region is observed to be consistently around 3.3 g/cm<sup>3</sup>. These high densities trigger a structural transformation of  $\alpha$ -quartz. This high density phase, however, is limited to the duration of the shock pulse (10 ps). The end of the shock pulse limits this transformation behavior and the tail of the pressure wave results in the reduction in the density of the material to bring the material back to near zero pressure. As a result, in contrast to that observed for fused silica, no permanent densification is observed at these pressures in  $\alpha$ -quartz at these shock pressures. Illustrative snapshots of the microstructure at the end of the shock pulse (10 ps) wherein the blue atoms are Si atoms and the green atoms are the O atoms. The snapshots reveal a crystalline microstructure with local reorientation during shock compression. The compressed material is returned to near zero pressure due to the propagation of the tail of the

shock wave. As a result, the snapshot in Fig. 12b shows a crystalline microstructure with reoriented grains of  $\alpha$ -quartz at a time of 15 ps. A peak value of tensile pressure of 15.2 GPa is observed at a time of 30 ps due to the interaction of the reflected tensile wave with the tail of the pressure wave as shown in the pressure profile in Fig. 11a. This peak tensile pressure, however, does not initiate spall failure of  $\alpha$ -quartz at an impact velocity of 2 km/s. Thus, no permanent densification or phase transformation is observed for  $\alpha$ -quartz at an impact velocity of 2 km/s.

Subjecting the  $\alpha$ -quartz sample to an impact of 3 km/s results in phase transformation behavior as observed for amorphous silica at 2 km/s. The pressure and density profile of  $\alpha$ -quartz for an impact velocity of 3 km/s are shown in Fig. 11b, c, respectively. It can be seen that significantly high pressures (peak pressure of ~64 GPa) are generated in the sample behind the shock front that render permanent densification (as shown by the residual compressive pressure) and initiate a phase transformation to stishovite. The snapshot of the system at the end of the shock pulse for an impact velocity of 3 km/s is shown in Fig. 13a. However, the limited duration of the shock pulse of 10 ps limits the completion of this transformation and the material comprises of a fluid-like structure of high-

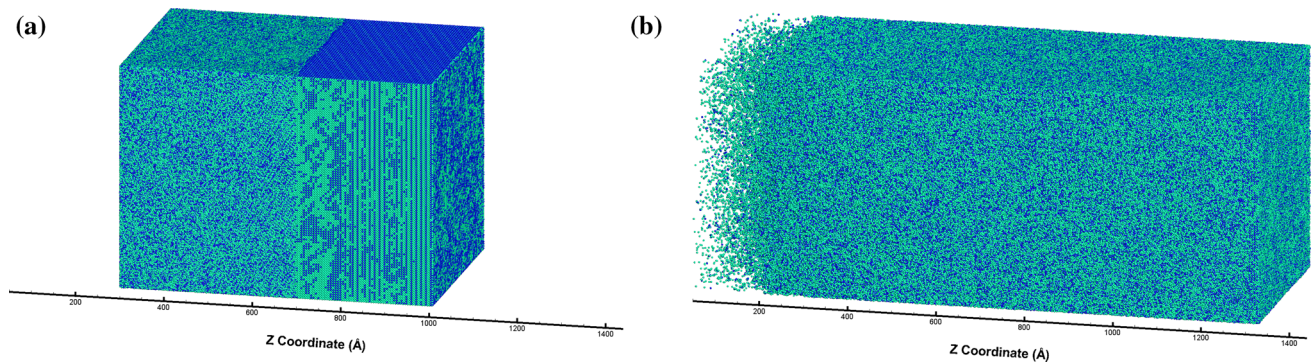


**Fig. 13** Evolution of the microstructure of  $\alpha$ -quartz during shock loading at an impact velocity of 3.0 km/s at times of **a** 10 ps and **b** 20 ps. The shock direction is shown by the *red arrow*. The *blue* atoms are Si atoms and the *green* atoms are the O atoms (Color figure online)

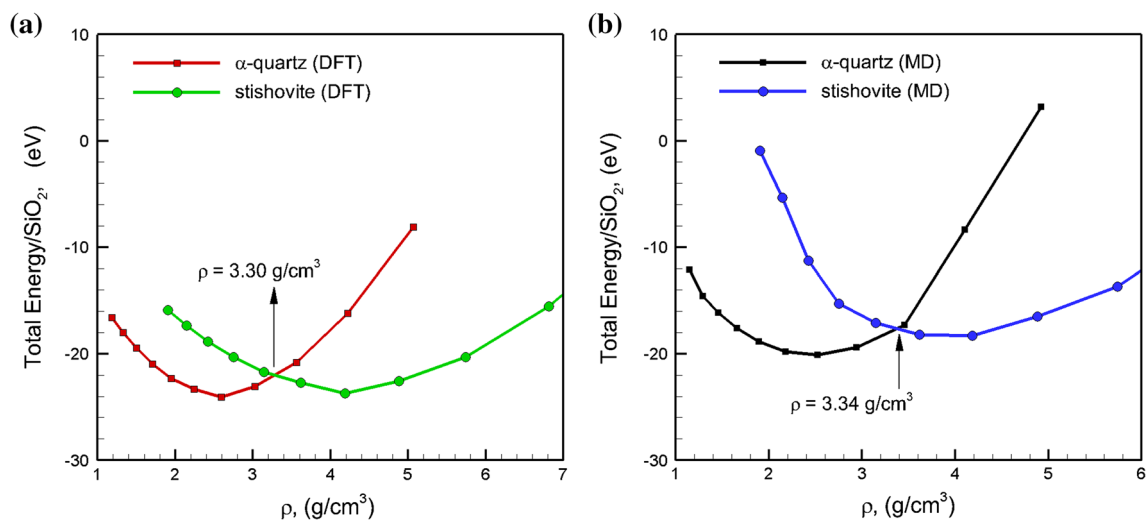


**Fig. 14** Plots of the energy of phases as a function of density for the  $\alpha$ -quartz and stishovite phases as computed using **a** DFT calculations and **b** using MD simulations with the Tersoff potential (Color figure online)

pressure silica. The propagation of the shock wave at such high pressures results in the ejection of material (as observed for amorphous silica) from the front end of the sample as shown in Fig. 13b. This ejection of the material is attributed to the relaxation of the material at the front end of the sample at the end of the pulse.

To understand the  $\alpha$ -quartz-to-stishovite phase transformation behavior, the variation of the energy for the  $\alpha$ -quartz and the stishovite phase per molecule of  $\text{SiO}_2$  as computed using DFT calculations is plotted as a function of density in Fig. 14a in comparison with that predicted by MD simulations using the Tersoff potentials in Fig. 14b. It can be seen from these plots that the DFT calculations predict that when  $\alpha$ -quartz is compressed to a density higher than  $3.30 \text{ g/cm}^3$ , the material prefers to transform to the stishovite phase as it has a lower energy as compared to  $\alpha$ -quartz. The MD simulations predict a similar trend, and the density at which the  $\alpha$ -quartz-to-stishovite transformation is energetically favorable is calculated to be  $3.34 \text{ g/}$

$\text{cm}^3$ . These results suggest that shock loading of  $\alpha$ -quartz with an impact velocity of 3 km/s results in permanent densification as well as a phase transformation to the high-pressure stishovite phase. The shock pressures required to induce densification and phase transformation agree very well with those observed experimentally.

The results presented here, therefore, demonstrate the capability of the Tersoff potential to model the shock-induced phase densification and phase transformation behavior of silica systems.

## Conclusions

Large-scale MD simulations are carried out to understand the wave propagation behavior, the permanent densification, as well as the phase transformation behavior in a- $\text{SiO}_2$  and  $\alpha$ -quartz as a function of shock pressure. For the case of amorphous silica, the impact velocities ranging from

500 m/s to 2 km/s and a pulse duration of 10 ps are used to generate planar shock waves with peak pressures up to 20 GPa behind the shock front. The planar wave profiles suggest that the width of both the shock front and the tail of the pressure wave change with the shock pressure. It is observed that the values of the average pressure of the material between the shock front and the tail of the pressure wave (and not the peak shock pressures) determine the densification and phase transformation behavior of the material as compared to peak shock pressures for impact velocities less than 1.5 km/s for amorphous silica. At these impact velocities, the propagation of tail of the shock wave returns the shock compressed region to near zero pressure. An impact velocity of 2 km/s generates peak shock pressures above  $\sim 20$  GPa and average pressures greater than 9 GPs in the compressed material. These pressures result in permanent densification of the material during compression even after the propagation of the tail of the pressure wave through the material as indicated by the residual compressive pressure behind the shock wave. In addition, shock pressures of  $\sim 20$  GPa lead to a phase transformation to a high-pressure stishovite phase as well as melting of part of the material in the shock compressed region. The shock pressures that result in the permanent densification and the melting of  $\alpha$ -SiO<sub>2</sub> are consistent with those observed experimentally. For all the impact velocities considered, the spall failure of  $\alpha$ -SiO<sub>2</sub>, however, is not observed as the peak tensile pressures generated do not exceed the spall strength computed using uniaxial expansion simulations at the relevant strain rates. These results demonstrate the ability of the Tersoff potential to predict the shock response of  $\alpha$ -SiO<sub>2</sub> at the atomic scales.

For the case of  $\alpha$ -quartz, MD simulations of shock loading of  $\alpha$ -quartz for an impact velocity of 2 km/s, i.e., peak shock pressures of  $\sim 22$  GPa and average shock pressure of  $\sim 15$  GPa in the compressed material do not allow for permanent densification of the material or phase transformation to the stishovite phase. A higher impact velocity of 3 km/s generates a peak pressure of  $\sim 64$  GPa that results in permanent densification as well as a transformation to the high-pressure stishovite phase. However, the small time scales of the shock compression do not allow for a complete transformation to stishovite and hence the microstructure corresponds to a more fluid-like structure as observed experimentally. The energetics of the various transformations is confirmed using DFT calculations.

These results demonstrate the ability of the Tersoff potential to model the structural transformations in SiO<sub>2</sub> under shock-loading conditions. Thus, the Tersoff potential is able to reproduce the shock response of  $\alpha$ -SiO<sub>2</sub> and  $\alpha$ -quartz as observed experimentally. The results are also relevant in the understanding of the shock response of

silicate glasses with SiO<sub>2</sub> as the primary constituent in the chemical composition such as silicate-based glass compositions for transparent armor applications.

**Acknowledgements** The research was sponsored by the University of Connecticut Research Foundation (UCRF) through the Faculty Large Grant funding program. The authors also acknowledge the Booth Engineering Center for Advanced Technology (BECAT) high performance computing resources at the University of Connecticut used to carry out this research.

## References

1. Limiting transparent armor damage reduces cost and replacement burden (2014) In: TARDEC Public Affairs. <http://www.tacomcmccommunityreport.com/news/feb14news6.aspx>
2. Bridgman PW, Šimon I (1953) Effects of very high pressures on glass. *J Appl Phys* 24(4):405–413
3. Wackerle J (1962) Shock-wave compression of quartz. *J Appl Phys* 33(3):922–937
4. Hemley R, Mao H, Bell P, Mysen B (1986) Raman spectroscopy of SiO<sub>2</sub> glass at high pressure. *Phys Rev Lett* 57(6):747–750
5. Sugiura H (1981) Dynamic response of fused quartz in the permanent densification region. *J Appl Phys* 52(5):3375–3382
6. Sugiura H, Ikeda R, Kondo K, Yamadaya T (1997) Densified silica glass after shock compression. *J Appl Phys* 81(4):1651–1655
7. Zha C-S, Hemley R, Mao H-K, Duffy T, Meade C (1994) Acoustic velocities and refractive index of SiO<sub>2</sub> glass to 57.5 GPa by Brillouin scattering. *Phys Rev B* 50(18):13105–13112
8. Schmitt DR, Ahrens TJ (1989) Shock temperatures in silica glass: implications for modes of shock-induced deformation, phase transformation, and melting with pressure. *J Geophys Res* 94(B5):5851–5871
9. Grady DE, Murri WJ, Fowles GR (1974) Quartz to stishovite: wave propagation in the mixed phase region. *J Geophys Res* 79(2):332–338
10. Graham RA (1974) Shock-wave compression of x-cut quartz as determined by electrical response measurements. *J Phys Chem Solids* 35(3):355–372
11. Daw MS, Baskes MI (1984) Embedded-atom method: derivation and application to impurities, surfaces, and other defects in metals. *Phys Rev B* 29(12):6443–6453
12. Foiles SM (1985) Application of the embedded-atom method to liquid transition metals. *Phys Rev B* 32(6):3409–3415
13. Johnson RA (1988) Analytic nearest-neighbor model for fcc metals. *Phys Rev B* 37(8):3924–3931
14. Dongare AM, Rajendran AM, LaMattina B, Zikry MA, Brenner DW (2010) Atomic scale studies of spall behavior in nanocrystalline Cu. *J Appl Phys* 108(11):113518
15. Dongare AM, Rajendran AM, Lamattina B, Brenner DW, Zikry MA (2009) Atomic-Scale study of plastic-yield criterion in nanocrystalline Cu at high strain rates. *Metall Mater Trans A* 41(2):523–531
16. Dongare A, Rajendran A, LaMattina B, Zikry M, Brenner D (2009) Atomic scale simulations of ductile failure micromechanisms in nanocrystalline Cu at high strain rates. *Phys Rev B* 80(10):104103
17. Dongare AM, Rajendran AM, LaMattina B, Zikry MA, Brenner DW. Atomistic studies of void-growth based yield criteria in single crystal Cu at high strain rates. In: AIP conference proceedings, vol. 1195, pp 769–772

18. Dongare AM, LaMattina B, Rajendran AM (2011) Atomic scale studies of spall behavior in single crystal Cu. *Procedia Eng* 10:3636–3641
19. Valisetty RR, Dongare AM, Rajendran AM, Namburu RR (2013) Effect of the strain rate and microstructure on damage growth in aluminum. *Comput Mater Contin* 36(3):231–255
20. Tsuneyuki S, Tsukada M, Aoki H, Matsui Y (1988) First-principles interatomic potential of silica applied to molecular dynamics. *Phys Rev Lett* 61(7):869–872
21. van Beest BWH, Kramer GJ (1990) Force fields for silicas and aluminophosphates based on ab initio calculations. *Phys Rev Lett* 64(16):1955–1958
22. Barmes F, Soulard L, Mareschal M (2006) Molecular dynamics of shock-wave induced structural changes in silica glasses. *Phys Rev B* 73(22):224108
23. Farrow MR, Probert MI (2011) Atomistic molecular dynamics simulations of shock compressed quartz. *J Chem Phys* 135(4):044508
24. Munetoh S, Motooka T, Moriguchi K, Shintani A (2007) Interatomic potential for Si–O systems using Tersoff parameterization. *Comput Mater Sci* 39(2):334–339
25. Tersoff J (1988) New empirical approach for the structure and energy of covalent systems. *Phys Rev B* 37(12):6991–7000
26. Su R, Xiang M, Chen J, Jiang S, Wei H (2014) Molecular dynamics simulation of shock induced ejection on fused silica surface. *J Appl Phys* 115(19):193508
27. Plimpton S (1995) Fast parallel algorithms for short-range molecular dynamics. *J Comput Phys* 117(1):1–19
28. Beeman D (1976) Some multistep methods for use in molecular dynamics calculations. *J Comput Phys* 20(2):130–139
29. Brutzel LV, Rountree CL, Kalia RK, Nakano A, Vashishta P (2001) Dynamic fracture mechanisms in nanostructured and amorphous silica glasses million-atom molecular dynamics simulations. In: *MRS online proceedings library*, 703 null-null
30. Muralidharan K, Simmons JH, Deymier PA, Runge K (2005) Molecular dynamics studies of brittle fracture in vitreous silica: review and recent progress. *J Non Cryst Solids* 351(18):1532–1542
31. Mantsi B, Tanguy A, Kermouche G, Barthel E (2012) Atomistic response of a model silica glass under shear and pressure. *Eur Phys J B* 85(9):1–13
32. Yuan F, Huang L (2012) Molecular dynamics simulation of amorphous silica under uniaxial tension: from bulk to nanowire. *J Non Cryst Solids* 358(24):3481–3487
33. Muralidharan K, Oh K-D, Deymier PA, Runge K, Simmons JH (2007) Molecular dynamics simulations of atomic-level brittle fracture mechanisms in amorphous silica. *J Mater Sci* 42(12):4159–4169. doi:[10.1007/s10853-007-1638-2](https://doi.org/10.1007/s10853-007-1638-2)
34. Pedone A, Malavasi G, Menziani MC, Segre U, Cormack AN (2008) Molecular dynamics studies of stress–strain behavior of silica glass under a tensile load. *Chem Mater* 20(13):4356–4366
35. Kresse G, Furthmüller J (1996) Efficient iterative schemes for ab initio total-energy calculations using a plane-wave basis set. *Phys Rev B* 54(16):11169
36. Perdew JP, Burke K, Ernzerhof M (1996) Generalized gradient approximation made simple. *Phys Rev Lett* 77(18):3865–3868